BRIEF COMMUNICATION

A novel monoacylglycerol lipase-targeted ^{18}F-labeled probe for positron emission tomography imaging of brown adipose tissue in the energy network

Ran Cheng[1,2], Masayuki Fujinaga[3], Jing Yang[4], Jian Rong[1], Ahmed Haider[1], Daisuke Ogasawara[5], Richard S. Van[6], Tuo Shao[1], Zhen Chen[1], Xiaofei Zhang[1], Erick R. Calderon Leon[6], Yiding Zhang[3], Wakana Mori[3], Katsushi Kumata[3], Tomoteru Yamasaki[3], Lin Xie[3], Shaofa Sun[7], Lu Wang[1], Chongzhao Ran[4], Yihan Shao[6], Benjamin Cravatt[5], Lee Josephson[1], Ming-Rong Zhang[3] and Steven H. Liang[1]

Monoacylglycerol lipase (MAGL) constitutes a serine hydrolase that orchestrates endocannabinoid homeostasis and exerts its function by catalyzing the degradation of 2-arachidonoylglycerol (2-AG) to arachidonic acid (AA). As such, selective inhibition of MAGL represents a potential therapeutic and diagnostic approach to various pathologies including neurodegenerative disorders, metabolic diseases and cancers. Based on a unique 4-piperidinyl azetidine diamide scaffold, we developed a reversible and peripheral-specific radiofluorinated MAGL PET ligand [18F]FEPAD. Pharmacokinetics and binding studies on [18F]FEPAD revealed its outstanding specificity and selectivity towards MAGL in brown adipose tissue (BAT) – a tissue that is known to be metabolically active. We employed [18F]FEPAD in PET studies to assess the abundancy of MAGL in BAT deposits of mice and found a remarkable degree of specific tracer binding in the BAT, which was confirmed by post-mortem tissue analysis. Given the negative regulation of endocannabinoids on the metabolic BAT activity, our study supports the concept that dysregulation of MAGL is likely linked to metabolic disorders. Further, we now provide a suitable imaging tool that allows non-invasive assessment of MAGL in BAT deposits, thereby paving the way for detailed mechanistic studies on the role of BAT in endocannabinoid system (ECS)-related pathologies.

Keywords: monoacylglycerol lipase (MAGL); positron emission tomography (PET); diagnostic imaging; fluorine-18; brown adipose tissue (BAT)

INTRODUCTION

Monoacylglycerol lipase (MAGL), a 33 kDa serine hydrolase, is a key degrading enzyme of 2-arachidonoylglycerol (2-AG) in the endocannabinoid system and releases arachidonic acid (AA) in the central nervous system (CNS) and peripheral tissues, such as brain, liver, lung and adipose tissues. Blockade of MAGL increases the level of 2-AG and lowers AA release, which not only affects cognitive processes and provides neuroprotection against neurodegenerative diseases [1–5], but also acts as a critical element in the control of inflammatory syndromes, cancer pathogenesis, obesity, and energy metabolism [6–11]. Along this line, visualization and quantification of expression and biological activity of MAGL with an appropriate diagnostic imaging tool represents an unmet medical need in the disease detection and staging, as well as assessment of response to MAGL-mediated therapy.

Positron emission tomography (PET) is a nuclear imaging technique that enables in vivo visualization and quantification of
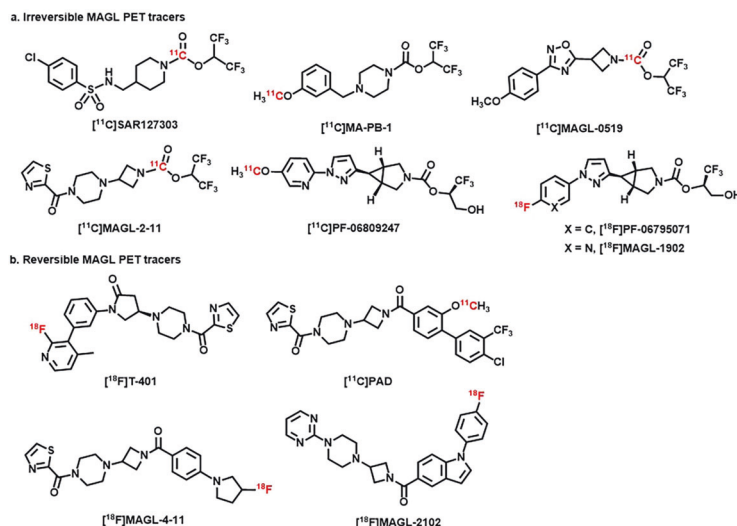
biochemical and pharmacological processes at the molecular level. A sensitive and specific positron-emitting probe can provide valuable functional information on target expression under normal and disease conditions, and further support drug discovery efforts by allowing non-invasive target engagement of MAGL inhibitors in preclinical and clinical development. Accordingly, strenuous efforts have been made to develop suitable targeted probes to visualize MAGL [12]. Initial attempts have led to the discovery of several probes with high in vitro target affinity but insufficient brain uptake or limited in vivo specificity. These probes included [11C]KML29, [11C]JW642, [11C]ML30 and [11C]JJKK-0048 [13]. Recently, several promising MAGL probes have been successfully advanced to PET imaging studies and showed reasonable brain uptake and specificity in vivo (Fig. 1) [14]. Besides the reported irreversible probes (Fig. 1a), which operate via the formation of covalent bonds by acylation of reactive cysteine/serine residues, PET probes with reversible binding properties (Fig. 1b) would allow kinetic modeling

A novel MAGL-targeted ^{18}F-labeled probe for PET imaging of BAT
R Cheng et al.

3003

Fig. 1 **Reported irreversible and reversible MAGL PET ligands. a** Irreversible MAGL PET tracers; **b** Reversible MAGL PET tracers.

studies to obtain critical information on distribution volume and binding potential, which constitute key parameters for quantitative PET imaging [15, 16]. To date, only few reversible PET tracers have been disclosed by our group and others, namely, [18F]T-40 [17], [11C]PAD and [18F]MAGL-4-11 [18] (Fig. 1b). In addition to those probes, we have recently identified a novel piperazinyl azetidine-based MAGL PET tracer, [18F]MAGL-2102, that exhibited in vivo performance characteristics. Indeed, [18F]MAGL-2102 showed a reversible binding mechanism and was successfully employed to visualize MAGL in the non-human primate (NHP) brain [19]. Nonetheless, it should be noted that previous imaging efforts have been limited to neurological applications in the CNS, while MAGL imaging studies on peripheral application are scarce.

Compared to the radioisotope carbon-11 (^{11}C, $t_{1/2}$ = 20.4 min), fluorine-18 (^{18}F) has a relatively longer half-life ($t_{1/2}$ = 109.7 min) and is more suitable for multistep synthesis, and restrained to radio-chemistry facilities equipped with cyclotron [20]. Recently, we developed a C-11 radiolabeled MAGL PET tracer [11C]PAD, which was based on a piperazinyl azetidine scaffold and exhibited reversible binding mechanism to MAGL (Fig. 1b). In order to introduce F-18 into [11C]PAD skeleton to replace C-11 to obtain a new F-18 radiolabeled reversible MAGL PET tracer, herein we described the discovery of a novel reversible and peripheral-specific radiofluorinated MAGL PET ligand, [18F]FEPAD ([18F]**4**), which was proved to be highly suited to visualize MAGL in peripheral tissues. Comprehensive pharmacological studies (potency, selectivity and reversible binding mechanism), PET imaging and ex vivo distribution of our lead molecule were performed to confirm the specificity in vivo. As proof-of-concept, we utilized this diagnostic tool to visualize and non-invasively quantify MAGL in the brown adipose tissue (BAT), a highly active metabolic tissue that has been shown to be regulated by the endocannabinoid system [21, 22]. We found a remarkably high and specific tracer accumulation in the BAT by in vivo imaging, which was confirmed by ex vivo analysis. Non-invasive assessment of MAGL activity and abundancy in the BAT constitutes a promising concept to elucidate the role of the endocannabinoid system in energy regulation and metabolic disorders in humans. Further, our findings might shed light on how MAGL inhibitors modulate lipid metabolism in cancer malignancy, neurological and metabolic disorders [23].

MATERIALS AND METHODS
The general procedure for experimental section was described previously with minor modification in this work [24]. All the

starting materials used in the synthesis were purchased from commercial vendors and used without further purification. Thin-layer chromatography (TLC) was conducted with 0.25 mm silica gel plates ([60]F[254]) and visualized by exposure to UV light (254 nm) or stained with potassium permanganate. Flash column chromatography was performed using silica gel (particle size 0.040–63 mm). [1]H-Nuclear magnetic resonance (NMR) spectra were obtained on a 300 MHz on Bruker spectrometers. ^{13}C NMR spectra were obtained at 75 MHz. ^{19}F NMR spectra were obtained at 282 MHz. Chemical shifts (δ) were reported in ppm and coupling constants were reported in Hertz. The multiplicities are abbreviated as follows: s = singlet, d = doublet, t = triplet, q = quartet, quint = quintet, sext = sextet, sept = setpet, m = multiplet, br = broad signal, dd = doublet of doublets. For all HRMS measurements, the ionization method was ESI and the mass analyzer type was TOF. Melting point was measured by Thomas Hoover capillary melting point apparatus (PA, USA). Fluorine-18, was produced by a GE PETtrace cyclotron (16.5 MeV) or a SUMITOMO CYPRIS HM-18 cyclotron. The animal experiments were approved by the Institutional Animal Care and Use Committee of Massachusetts General Hospital or the Animal Ethics Committee at the National Institute of Radiological Sciences (Japan). All animal procedures were performed in accordance with the guidelines of the Institutional Animal Care and Use Committee of Massachusetts General Hospital or the Animal Ethics Committee at the National Institute of Radiological Sciences (Japan). DdY mice (male; 5–7 weeks, 34–36 g) and BALB/c mice (female, 5–7 weeks, 18–24 g) were purchased from Charles River Laboratory (Wilmington, USA) or Japan SLC (Shizuoka, Japan), and kept on a 12 h light/12 h dark cycle and were allowed food and water *ad libitum*.

Chemical synthesis of MAGL-targeted molecules
The starting materials **1** and **2** were prepared according to our published procedures [18]. FEPAD (**4**) was obtained within two steps as a white solid (for detailed procedure, please see Supplementary Information, SI).

MAGL and FAAH substrate hydrolysis assays
MAGL and FAAH substrate hydrolysis measurements were determined according to the previously reported LC-MS-based assay [25]. hMAGL/hFAAH1-transfected HEK293T proteomes (1.0 μg for hMAGL and 10 μg for hFAAH1) in 80 μL of DPBS was used for measuring substrate hydrolysis activity. A 20 μL of 0.25 mM substrate (50 μM final concentration) was incubated with the enzyme solution with DMSO or inhibitor for 15 min at room

3004

temperature (for hMAGL), or for 30 min at 37 °C (for hFAAH1). The reactions were quenched by the addition of 400 μL of 2:1 (v/v) CHCl₃:MeOH, doped with 1 nmol AA-d8, vortexed, then centrifuged (1400 × g, 3 min) to separate the phases.

A 20 μL of the resultant organic phase was injected onto an Agilent 6100 series Quadrupole LC/MS instrument. LC separation was achieved with a Gemini reverse phase C18 column (50 mm × 4.6 mm with 5 μm diameter particles, Phenomenex). Mobile phase A was made of 95:5 (v/v) H₂O:MeOH, and mobile phase B was made of a 65:35:5 (v/v/v) i-PrOH:MeOH:H₂O + 0.1% ammonium hydroxide was included to assist in ion formation in negative ionization mode. The flow rate was 0.4 mL/min and the gradient consisted of 1 min 20% B, followed by an isocratic gradient of 100% B for 7 min before equilibrating for 3 min at 20% B.

In vitro human recombinant MAGL enzyme inhibition assay

IC₅₀ values of the testing compound FEPAD were determined according to our previous report [24] and manufacturer's instructions from commercially available MAGL screening kits (Cayman Chemical, Ann Arbor, MI, USA, Item No. 705192), which containing human recombinant MAGL, 4-nitrophenylacetate substrate (4-NPA; 4.25 mM ethanol solution), MAGL assay buffer (10×), JZL 195 inhibitor, 96-well plate and 96-well cover sheet. The reported MAGL inhibitor JZL 195 was used as a reference. The IC₅₀ values for compounds were generated in 96-well plates. We diluted 3 mL of assay buffer with 27 mL of HPLC-grade water. This final 1× assay buffer (10 mM Tris-HCl, pH 7.2, containing 1 mM EDTA) should be used in the assay and for the dilution of MAGL. We diluted 30 μL of MAGL with 570 μL of 1× MAGL assay buffer and added 10 μL of this solution to 150 μL of 1× assay buffer in each well followed by 10 μL of DMSO containing the appropriate amount of inhibitor or JZL 195. After a 10 min incubation at room temperature, the reactions were initiated by adding 10 μL of MAGL substrate to all the wells being used. The final volume of the assay was 180 μL in all the wells. The 96-well plate was carefully shaked for 10–20 s to mix and covered with the plate cover. It was incubated for 20 min at room temperature. The absorbance values were then measured at 405–15 nm. Two reactions were also included: one reaction containing no inhibitors and the second one containing neither inhibitor nor enzyme. IC₅₀ values were derived from experimental data using dose-response simulation function in GraphPad Prism.

In vitro human recombinant FAAH enzyme inhibition assay

IC₅₀ values of testing compound FEPAD were determined according to our previous report [24] and manufacturer's instructions from commercially available FAAH screening kits (Cayman Chemical, Ann Arbor, MI, USA, Item No. 1005196), which containing human recombinant FAAH, FAAH substrate (400 μM AMC arachidonoyl amide), FAAH assay buffer (10×), JZL 195 inhibitor, 96-well plate (black) and 96-well cover sheet. The reported FAAH inhibitor JZL 195 was used as a reference. The IC₅₀ values for compounds were generated in 96-well plates. FAAH hydrolyzes AMC arachidonoyl amide resulting in the release of the fluorescent product, 7-amino-4-methylcoumarin (AMC). The fluorophore can be easily analyzed using an excitation wavelength of 340–60 nm and an emission wavelength of 450–65 nm. We diluted 3 mL of assay buffer with 27 mL of HPLC-grade water. This final 1× assay buffer (125 mM Tris-HCl, pH 9.0, containing 1 mM EDTA) should be used in the assay and for the dilution of FAAH. We diluted 120 μL of FAAH with 480 μL of 1× FAAH assay buffer and added 10 μL of this solution to 170 μL of 1× assay buffer in each well followed by 10 μL of DMSO containing the appropriate amount of inhibitor or JZL 195. After a 10 min incubation at 37 °C, the reactions were initiated by adding 10 μL of FAAH substrate to all the wells being used. The final volume of the assay was 200 μL in all the wells. The 96-well plate was carefully shaked for 10–20 s to mix and covered with the plate cover. It was incubated for

30 min at 37 °C. The plate cover was removed and the plate was read using an excitation wavelength of 340–60 nm and an emission wavelength of 450–65 nm. Two reactions were also included: one reaction containing no inhibitors and the second one containing neither inhibitor nor enzyme. IC₅₀ values were derived from experimental data using dose-response simulation function in GraphPad Prism.

Activity-based protein profiling (ABPP)

The general procedure for ABPP assay was described previously [26, 27]. In brief, mouse brain membrane proteomes (1 mg/mL) were preincubated with either DMSO or inhibitors (1 μM) at 37 °C. After 30 min, FP-rhodamine (1 μM or 500 nM final concentration) was added and the mixture was incubated for another 1 to 180 min at room temperature. Reactions were quenched with 4× SDS loading buffer and run on SDS-PAGE. Samples were visualized by in-gel fluorescence scanning using a ChemiDoc MP system. The percentage of enzyme activity remaining was determined by measuring the integrated optical intensity of the fluorescent protein bands using Image Lab 5.2.1. The relative intensity was compared to the DMSO treated proteomes, which were set to 100%.

Pharmacological evaluation on CB₁ and CB₂ receptors

CB₁ and CB₂ binding profiles of compound FEPAD (**4**) were determined according to published literatures [24, 26, 28] and supported by the National Institute of Mental Health's Psychoactive Drug Screening Program. The detailed procedures "assay protocol book" are listed on the website (https://pdsp.unc.edu/pdspweb/).

Molecular docking study

Computational studies. The calculations in this work were performed using UCSF Chimera 1.15, IQmol 2–14.0, and AutoDock Vina 1.1.2 on a computer with Intel Quad Core i7–7500U CPU @ 2.70 GHz.

Ligand and receptor preparation. The ligand structure was built and optimized using IQmol. The receptor structure (PDB: 3PE6) was loaded in UCSF Chimera, and the original inhibitor was removed. The receptor structure was then prepared for docking through Dock Prep, which deleted the solvent, added hydrogen atoms, and assigned atomic partial charges. For standard residues, AMBER ff14SB charges were used, while Gasteiger charges were assigned for nonstandard residues.

Docking. AutoDock Vina was used to dock the ligand to the receptor. The initial docking was conducted by constructing a box encompassing the entire protein and finding the best (global) docking position within that box. Then, around the pocket for the lowest-energy global binding pose, a smaller box of 30 Å × 30 Å × 30 Å was used for the subsequent docking to refine the docking pose.

Radiosynthesis of MAGL-targeted molecules

Radiosynthesis of [18F]FEPAD ([18F]**4**) using 1-bromo-2-[18F]fluoroethane: The general procedure was described previously [24, 26, 28] with minor modification in this work. [18F]Fluoride was first trapped on a QMA carbonate ion exchange solid phase extraction cartridge, and then eluted into a reaction vial with a solution containing K₂CO₃ (2.75 mg) and kryptofix 222 (8.25 mg) in CH₃CN/H₂O (400 μL, v/v, 1/1). The reaction mixtures were dried azeotropically to remove H₂O and CH₃CN at 110 °C for 15 min. To the reaction vial, 2-bromoethyl trifluoromethanesulfonate (10 μL) in 1,2-dichlorobenzene (150 μL) was added and heated at 130 °C for 2 min, followed by distillation via N₂ gas (50 mL/min) to isolate 1-bromo-2-[18F]fluoroethane. The [18F] reagent was dissolved in a solution of phenolic precursor **3** (1.5 mg) and NaOH (5.8 μL, 0.5 M) in

A novel MAGL-targeted ^{18}F-labeled probe for PET imaging of BAT
R Cheng et al.

3005

DMF (250 μL) at −20 °C, then heated at 85 °C for 10 min. HPLC buffer (CH$_3$CN/H$_2$O/Et$_3$N, v/v/v, 6/4/0.01, 0.5 mL) was added to the reaction mixture, which was then injected into a semi-preparative HPLC system. HPLC purification was completed on a Capcell Pak C$_{18}$ column (10 mm ID × 250 mm) using a mobile phase of CH$_3$CN/H$_2$O/Et$_3$N (v/v/v, 6/4/0.01) at a flowrate of 5.0 mL/min. The retention time for [18]FFEPAD was 8.8 min. The product was collected in a sterile flask, evaporated to dryness in vacuo, re-dissolved in a saline solution (3 mL) containing 100 μL of 25% ascorbic acid in sterile water and 100 μL of 20% Tween® 80 in ethanol. The synthesis time was ca. 61 min from end-of-bombardment. The identity, radiochemical and chemical purity of [18]FFEPAD ([18]F**4**) were determined by the co-injection with unlabeled FEPAD by an analytical HPLC method (Capcell Pak C$_{18}$, 4.6 mm ID × 250 mm, UV at 254 nm; CH$_3$CN/H$_2$O/Et$_3$N (v/v/v, 6/4/0.01); retention time 8.4 min, 1.0 mL/min). Radiochemical yield was 13% ± 4% (decay-corrected) based on [^{18}F]fluoride with more than 99% radiochemical purity and greater than 3 Ci/μmol molar activity.

Radiosynthesis of [18]FFEPAD ([18]F**4**) using 2-[^{18}F]fluoroethyl tosylate: The general procedure was described previously [24, 26, 28] with minor modification in this work. Using 1,2-bis(tosyloxy)ethane as a template compound, [^{18}F]fluorination was performed and optimized under a comprehensive array of labeling conditions (Supplementary Table S1, SI). [^{18}F]Fluoride was first trapped on a QMA carbonate ion exchange solid phase extraction cartridge, and then eluted into a 5 mL V-shaped reaction vial with a solution containing K$_2$CO$_3$ (1 mg) and kryptofix 222 (5 mg) in CH$_3$CN/H$_2$O (1 mL, v/v, 7/3). The reaction mixtures were dried azeotropically to remove H$_2$O and CH$_3$CN at 110 °C for 15 min under a stream of nitrogen. The evaporation was repeated three times with the addition of dry acetonitrile (1 mL) each time. After that, the dried [^{18}F]fluoride was re-dissolved in 0.4 mL of dry MeCN. To the reaction vial, 1,2-bis(tosyloxy)ethane (5 mg) and a magnetic stirrer bar were added. The vial was sealed and heated at 125 °C for 10 min. After the reaction was completed, mixture aliquot (2–5 μL) was taken for analysis by radioTLC (eluent: ethyl acetate) for radiochemical conversion (RCC). The solution was diluted with mobile phase (50% CH$_3$CN, 50% 0.1 M NH$_4$·HCO$_3$ (aq.), 3 mL) and filtered. The radiolabeling product [^{18}F]2-fluoroethyl 4-methylbenzenesulfonate was purified from semi-prep radio-HPLC. HPLC purification was completed on a Phenomenex luna 5 μm C$_{18}$(2) 100 Å 250 mm × 10.00 mm column using a mobile phase of CH$_3$CN/0.1 M NH$_4$·HCO$_3$ (aq.) (v/v, 5/5) at a flowrate of 5.0 mL/min. The retention time for 2-[^{18}F]fluoroethyl tosylate was 8.2 min. The radioactive fraction corresponding to the desired product was collected and diluted with 20 mL of H$_2$O. The mixture was then loaded onto a C$_{18}$ SPE cartridge (preactivated with 5 mL of EtOH followed by 10 mL of H$_2$O). The cartridge was washed with 20 mL of H$_2$O and dried by nitrogen gas for 3 min. The product [^{18}F]2-fluoroethyl tosylate was then eluted with 2.0 mL of CH$_3$CN into a 5 mL V-shaped reaction vial, evaporated to dryness by nitrogen gas at 60 °C for 15 min, and re-dissolved in 0.3 mL of dry DMF.

To the reaction vial, phenolic precursor **3** (2 mg), K$_2$CO$_3$ (2 mg) and a magnetic stirrer bar were added. The vial was sealed and heated at 130 °C for 10 min. After the reaction was completed, mixture aliquot (2–5 μL) was taken for analysis by radioTLC (eluent: ethyl acetate) for radiochemical conversion (RCC). The solution was diluted with mobile phase (60% CH$_3$CN, 40% 0.1 M NH$_4$·HCO$_3$ (aq.), 3 mL) and filtered. The radiolabeling product [18]FFEPAD ([18]F**4**) was purified from semi-prep radio-HPLC. HPLC purification was completed on a Phenomenex luna 5 μm C$_{18}$(2) 100 Å 250 mm × 10.00 mm column using a mobile phase of CH$_3$CN/0.1 M NH$_4$·HCO$_3$ (aq.) (v/v, 6/4) at a flowrate of 5.0 mL/min. The retention time for [18]FFEPAD was 13.8 min. The radioactive fraction corresponding to the desired product was collected and diluted with 13 mL of H$_2$O. The mixture was then loaded onto a C$_{18}$ SPE cartridge (preactivated with 5 mL of EtOH followed by 10 mL of H$_2$O). The cartridge was washed with 20 mL of H$_2$O and dried by

nitrogen gas for 3 min. The product [18]FFEPAD ([18]F**4**) was then eluted with 2.0 mL of CH$_3$CN and collected in a sterile flask, evaporated to dryness by nitrogen gas at 70 °C for 20 min, and reformulated in a saline solution (3 mL) containing 100 μL of 25% ascorbic acid in H$_2$O and 100 μL of 20% Tween 80 in ethanol. The synthesis time was ca. 160 min from end-of-bombardment. The identity, radiochemical and chemical purity of [18]FFEPAD were determined by the co-injection with unlabeled FEPAD by an analytical HPLC method (Supplementary Fig. S1, SI, Phenomenex luna 5 μm C18 100 Å 250 mm × 4.60 mm column, UV at 254 nm; CH$_3$CN/0.1 M NH$_4$·HCO$_3$ (aq.) (v/v, 6/4); retention time 10.5 min, 1.0 mL/min). Radiochemical yield was 8% ± 2% (non-decay-corrected) with more than 99% radiochemical purity and greater than 1.5 Ci/μmol molar activity.

Small-animal PET study in rodents
The general procedure was described previously [24, 26, 28] with minor modification in this work. In brief, PET scans were conducted by a Sofie G4 scanner for mice studies. BALB/c mice were kept under anesthesia with 1%-2% (v/v) isoflurane during the scan. The radiotracer (25–35 μCi) was injected via a preinstalled catheter via the tail vein. Using Sofie G4 scanner, two 10 min static PET scans at 30 min and 60 min post injection were conducted. For all imaging experiments, mice were anesthetized using 1%−2% isoflurane in O$_2$ at a flow rate of ~1.5 L/min, positioned in a prone position along the long axis of the microPET scanner and imaged. Images were reconstructed using a filtered back projection reconstruction algorithm. For image analysis, cylindrical regions of interest (ROIs) were manually drawn from three-dimensional filtered back projection (FBP) reconstructed PET images using AMIDE software.

For pretreatment studies, PAD (3 mg/kg) or KML29 (3 mg/kg) dissolved in 300 μL saline containing 10% ethanol and 5% Tween® 80 was injected via the tail vein catheter 1 min before the injection of [18]FFEPAD. The radioactivity was decay-corrected and expressed as the standardized uptake value (SUV). SUV = (radioactivity per mL tissue / injected radioactivity) × body weight.

Ex vivo whole body biodistribution in mice
The general procedure was described previously [24, 26, 28] with minor modification in this work. In brief, a formulated solution of [18]FFEPAD (50 μCi/200 μL) was injected into DdY mice via the tail vein. Three mice were sacrificed at 1, 5, 15, 30, 60 min for the ^{18}F-tracer post injection. Major organs, including whole brain, heart, liver, lung, spleen, kidneys, adrenal glands, white/brown adipose tissue, small intestine (including contents), muscle, testes, and blood samples were quickly harvested and weighted in the baseline studies. Mouse BAT is a whole mass tissue and has a unique triangular physical shape which is easy to distinguish from other organs and tissues. BAT locates in interscapular area of mouse. The location is shallow and is situated away from larger organs such as the heart, liver, and stomach. For pretreatment studies, PAD (3 mg/kg) or KML29 (3 mg/kg) dissolved in 300 μL saline containing 10% ethanol and 5% Tween® 80 was injected via the tail vein catheter 1 min before the injection of [18]FFEPAD. Three-five mice were sacrificed at 30 min post injection. Brown adipose tissue and adrenal glands were harvested and weighed in the pretreatment experiments. The same procedure was used for BALB/c mice except only white/brown adipose tissues were harvested. The radioactivity in these organs was measured by a 1480 Wizard autogramma counter. The results were expressed as the percentage of injected dose per gram of wet tissue (% ID/g) or standardized uptake value (SUV). All radioactivity measurements were decay-corrected.

Radiometabolite analysis in plasma
The general procedure was described previously [24, 26, 28, 29] with minor modification in this work. In brief, following the intravenous injection of [18]FFEPAD (100 μCi/200 μL), DdY mice (n = 3) were sacrificed at 30 min. The blood samples were

centrifuged at $15,000 \times g$ for 2 min at 4 °C to separate the plasma. The supernatant (0.5 mL) was then collected in a test tube containing CH_3CN (0.5 mL) and the resulting mixture was vortexed for 15 s and centrifuged at $15,000 \times g$ for 2 min for deproteinization. An aliquot of the supernatant (100 μL) obtained from the plasma was injected into the radio-HPLC system, and analyzed under the same analytical conditions described above, except the flow rate of 2 mL/min. The percentage of [^{18}F]FEPAD to total radioactivity (corrected for decay) on the HPLC charts was calculated as (peak area for [^{18}F]FEPAD/total peak area) ×100.

Cherenkov luminescence imaging (CLI) studies
The general procedure was described previously [29] with minor modification in this work. In brief, BALB/c mice were anesthetized with isoflurane balanced with oxygen for 3 min and injected with [^{18}F]FEPAD (45–49 μCi) intravenously. CLI imaging was performed using an IVIS®Spectrum animal imaging system (Perkin Elmer/ Caliper LifeSciences, Hopkinton, MA, USA). Injected mice were then subjected to luminescence imaging at 30, 60, and 90 min after [^{18}F]FEPAD injection with the following parameters: open filter, f = 1, bin = 8, FOV = D, and exposure time = 120 s. Image analysis was conducted using LivingImage® 4.2 software.

Histological and immunohistochemistry
The general procedure was described previously [29–31] with minor modification in this work. In brief, interscapular white adipose tissue (WAT) and BAT specimens were fixed in 10% neutral buffered formalin, embedded in paraffin and cut into 4 μm sections. Specimens were dewaxed, hydrated, and stained usual method with standard hematoxylin and eosin (H&E) and analyzed by light microscopy. For immunohistochemistry (IHC), sections were incubated for 10 min in 3% hydrogen peroxide to block endogenous peroxidase. Antigen retrieval was performed by heating in 10 mM sodium citrate buffer (pH 6.0) for 10 min or incubation with pepsin for 10 min. Sections were treated with Dako protein block (X9090; Dako Envision, Dako) for 30 min and incubated with primary antibody MAGL (Abcam, Cambridge, MA, USA) at 4 °C overnight. Other sections were also incubated at 4 °C overnight in non-immune sera to demonstrate staining specificity. Polymer horseradish peroxidase (HRP) anti-rabbit (Invitrogen, Carlsbad, CA, USA) was used as secondary antibody. 3,3′-diaminobenzidine (DAB) was employed in the detection procedure [32]. Images were quantified by ImageJ software. ImageJ software was designed at National Institute of Health as open tools for the analysis of scientific images.

Immunofluorescent staining of FFPE tissue
Formalin-fixed paraffin embedded (FFPE) tissue was processed for staining. Following deparaffinization, antigen retrieval was performed in unmasking solution (Vector Laboratories, Burlingame, CA, USA) for 20 min at 125 °C in microwave. Unreacted aldehydes were quenched for 10 min with 1% $NaBH_4$. Prior to blocking, ImageIT enhancer (Invitrogen, Carlsbad, CA, USA) was applied to each section. Non-specific antibody binding was blocked with either 1% IgG-free BSA or 5% Normal donkey serum (Jackson Immuno, West Grove, PA, USA) in TBS (Tris-buffered saline), depending on the antibodies used. Primary antibodies were incubated overnight at 4 °C. Sections were washed with TBS and AlexaFluor-conjugated secondary antibodies (Invitrogen) were applied for 30 min at room temperature. DAPI counterstain (Invitrogen) was used to image nuclei and slides were mounted with ProLong gold (Invitrogen) [33]. Primary antibody MAGL (Abcam, Cambridge, MA, USA) was used. Images were quantified by the ImageJ software.

Statistical analysis
Quantitative data were expressed as mean ± SD. Statistical comparisons were carried out by using a Student's two-tailed t-test. $^*P < 0.05$, $^{**}P < 0.01$, and $^{***}P < 0.001$.
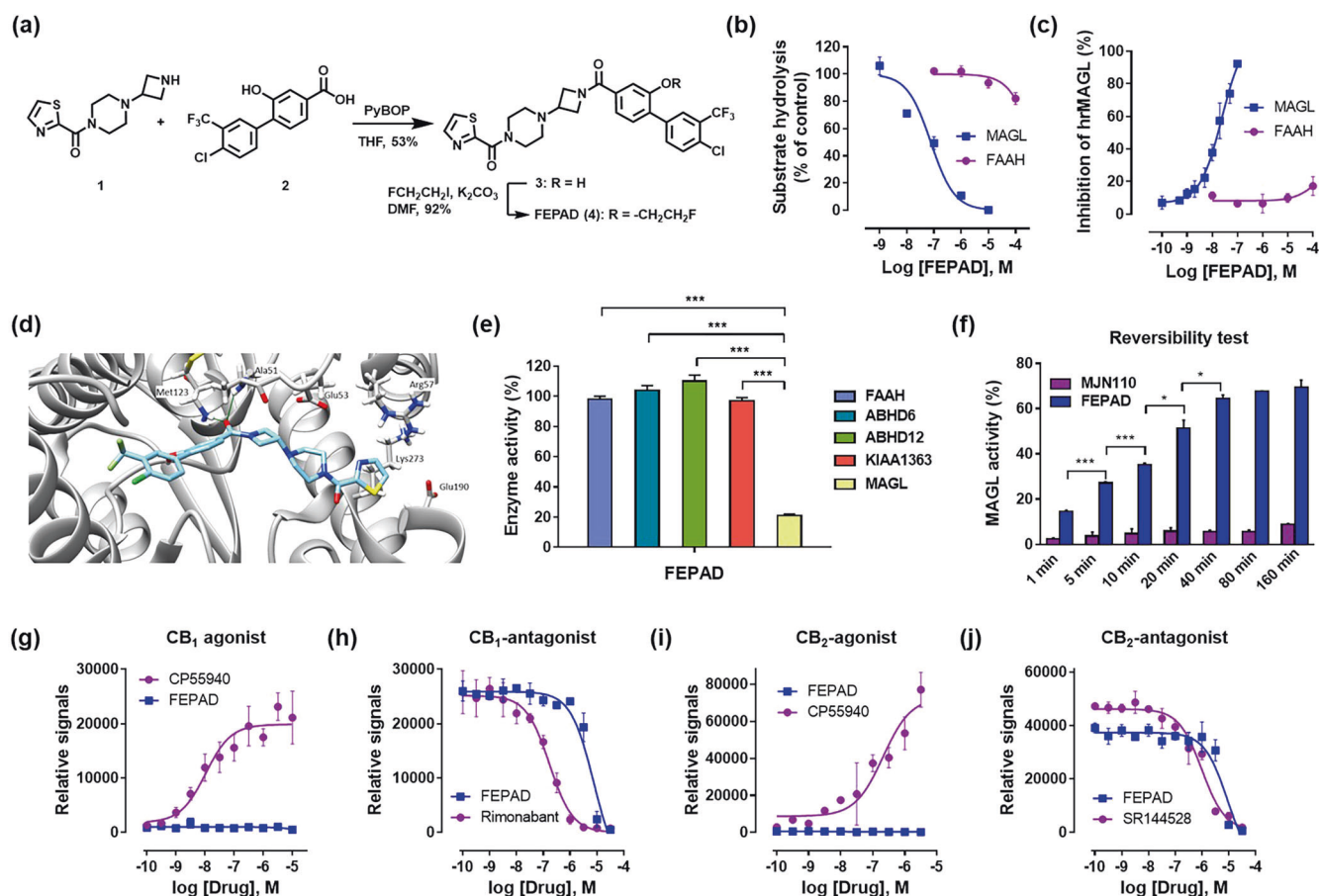
RESULTS

Synthesis and pharmacology of FEPAD
Our lead compound, (4-(1-(4′-chloro-2-(2-fluoroethoxy)−3′-(trifluor-omethyl)-[1,1′-biphenyl]−4-carbonyl)azetidin-3-yl)piperazin-1-yl) (thiazol-2-yl)methanone (FEPAD), possesses an azetidinyl piperazine scaffold [34] that exhibited high MAGL affinity and selectivity with reversible binding properties. FEPAD (**4**) was synthesized in a highly efficient and convergent manner. Briefly, the phenol **3** was obtained via condensation with amine **1** and carboxylic acid **2** in 53% yield, followed by alkylation, to give **4** in 92% yield (Fig. 2a). FEPAD showed strong binding affinities in vitro as determined by hydrolysis assay in hMAGL-expressing cell lines and recombinant hMAGL (Fig. 2b, c) with IC_{50} values of 77.6 ± 9.2 nM ($n = 3$) and 23.8 ± 4.9 nM ($n = 3$), respectively, with no significant interaction with FAAH (1000-fold selectivity). We established a molecular docking model to investigate possible interactions between FEPAD and MAGL that may contribute to the high affinity. The catalytic triad of MAGL, previously shown to consist of Ser_{122}, Asp_{239}, and His_{269}, was identified in the reported structure of a ligand-protein complex (PDB: 3PE6) [35–37]. The protein pocket is mostly hydrophobic, however, potential hydrogen bond interaction sites were observed between amide hydrogens of Met123 and Ala51 of the receptor and the ketone functionality of the ligand. Two positively charged side chains, Arg57 and Lys273, interacted with the thiazole ring, where negatively charged Glu53 and Glu190 interacted with piperazine of the ligand (Fig. 2d). We next performed activity-based protein profiling (ABPP) [27] to directly assess the functional state of serine hydrolases that are responsible for 2-AG hydrolysis. FEPAD exhibited no significant off-target bindings to other major serine hydrolases in the ECS, including FAAH, ABHD6, ABHD12, and KIAA1363 (Fig. 2e). FEPAD further showed reversible binding behavior towards MAGL in a time-dependent manner (Fig. 2f). No significant agonism or antagonism towards cannabinoid receptors CB_1 and CB_2 was observed (Fig. 2g–j), in which IC_{50} values were greater than 13 μM and 34 μM for CB_1 and CB_2 antagonist assays, respectively.

Radiosynthesis and whole body biodistribution of [^{18}F]FEPAD ([^{18}F]**4**)
Encouraged by our in vitro results, we next performed the labeling of FEPAD with fluorine-18. [^{18}F]FEPAD ([^{18}F]**4**) was synthesized in a two-step procedure (Fig. 3a). The fluorinating agent 1-bromo-2-[^{18}F]fluoroethane or 2-[^{18}F]fluoroethyl tosylate was reacted with phenolic precursor **3** to give [^{18}F]**4** in 8%–13% radiochemical yields with high radiochemical purity (>99%) and high molar activity (>1.5 Ci/μmol). The uptake, distribution and clearance of [^{18}F]FEPAD were investigated by whole body biodistribution in rodents (Fig. 3b). Of note, uptake patterns of [^{18}F]FEPAD were consistent with the distribution of MAGL [37], of which high expression was observed in the BAT, adrenal glands, liver and kidneys. Low brain permeability was also observed, which confirmed the peripherally-restricted distribution of [^{18}F]FEPAD.

In vivo PET studies and BAT visualization
To verify in vivo specificity of [^{18}F]FEPAD to MAGL, we performed blocking studies using the MAGL inhibitors, PAD (3 mg/kg) and KML29 (3 mg/kg) [34, 38], and determined uptake changes by ex vivo analysis. [^{18}F]FEPAD demonstrated significantly decreased uptake in two characteristic MAGL-rich tissues, i.e., 76%–81% reduction in BAT and 41%–51% decrease in adrenal glands under blocking conditions (Fig. 4a). While our reported C-11 tracer [^{11}C] PAD showed relatively lower blocking effect (50% decrease by PAD and 63% by KML29) in brown adipose tissue, the uptake in adrenal glands (7%–18% changes) was not substantially affected between control and inhibitory conditions (Supplementary Fig. S2, SI). We also carried out radiometabolite analysis and determined the percentage of unchanged parent fraction in plasma at 30 min post injection was 49%.

A novel MAGL-targeted ^{18}F-labeled probe for PET imaging of BAT
R Cheng et al.

3007

Fig. 2 FEPAD is a potent and selective MAGL reversible inhibitor. a Synthesis of FEPAD (**4**). Inhibition assay results of **4** based on **b** transiently expressed hMAGL and hFAAH in HEK293T cells or **c** recombinant hMAGL and hFAAH; **d** Overview of the MAGL protein (gray) in complex with **4** (light blue) in the ligand binding pocket. The best docking pose had a score of −12.3 kcal/mol. The H-bonds are represented as solid dark green lines; **e** Serine hydrolase selectivity determined by ABPP using mouse brain membrane proteomes; **f** Time-dependent reversible binding profile of **4** determined at different incubation time points with an irreversible inhibitor MJN110 as control. Recovered MAGL activity over time indicates the binding of **4** is reversible while irreversible MJN110 shows no significant time-dependent changes. **g** Agonism of **4** in the CB_1 assay with CP55940 as control; **h** Antagonism of **4** in the CB_1 assay with rimonabant as control; **i** Agonism of **4** in the CB_2 assay with CP55940 as control and **j** antagonism of **4** in the CB_2 assay with SR144528 as control. All data were mean ± SD, $n = 3-5$. $^*P < 0.05$, $^{***}P < 0.001$.
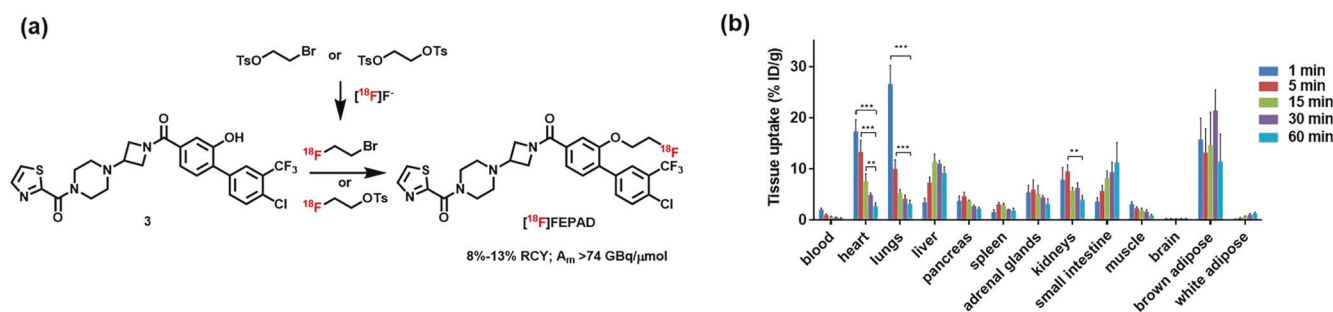

Fig. 3 Radiosynthesis and whole body biodistribution of [18F]FEPAD. a Radiosynthesis of [18F]FEPAD; **b** Ex vivo whole body biodistribution of [18F]FEPAD in mice at 1, 5, 15, 30 and 60 min post-injection in DdY mice. All data were mean ± SD, $n = 3-5$. $^{**}P < 0.01$, and $^{***}P < 0.001$.

We next analyzed and compared the uptake of [18F]FEPAD in the BAT and white adipose tissue (WAT) by PET imaging studies and ex vivo biodistribution analysis in rodents. As depicted in Fig. 4b–d, we observed characteristic BAT deposits and high uptake (2.1–7 SUV for interscapular BAT), low WAT uptake (0.6–1.1 SUV for interscapular WAT, and 0.20–6 SUV for inguinal WAT), as well as outstanding BAT/WAT uptake ratios. These findings were validated by ex vivo measurements (ca. 9–14 fold BAT:WAT ratio). As a complementary method [39] for PET imaging, we also use Cherenkov luminescence imaging (CLI) of [18F]FEPAD to profile

BAT. We observed significant CLI signals from the interscapular BAT and found an excellent correlation ($R^2 > 0.9$) between PET and CLI signals (Supplementary Fig. S3, SI).

The unique and high BAT uptake, as well as high BAT/WAT ratio of [18F]FEPAD encouraged us to investigate the relationship between MAGL distribution and adipose tissues. As shown in Fig. 4e, H&E staining showed a definite difference in cellular morphology, characterized by cell size and number and by the presence of multilocular adipocytes from BAT and unilocular cells from WAT. In particular, histological observations showed that

A novel MAGL-targeted ^{18}F-labeled probe for PET imaging of BAT
R Cheng et al.

3008
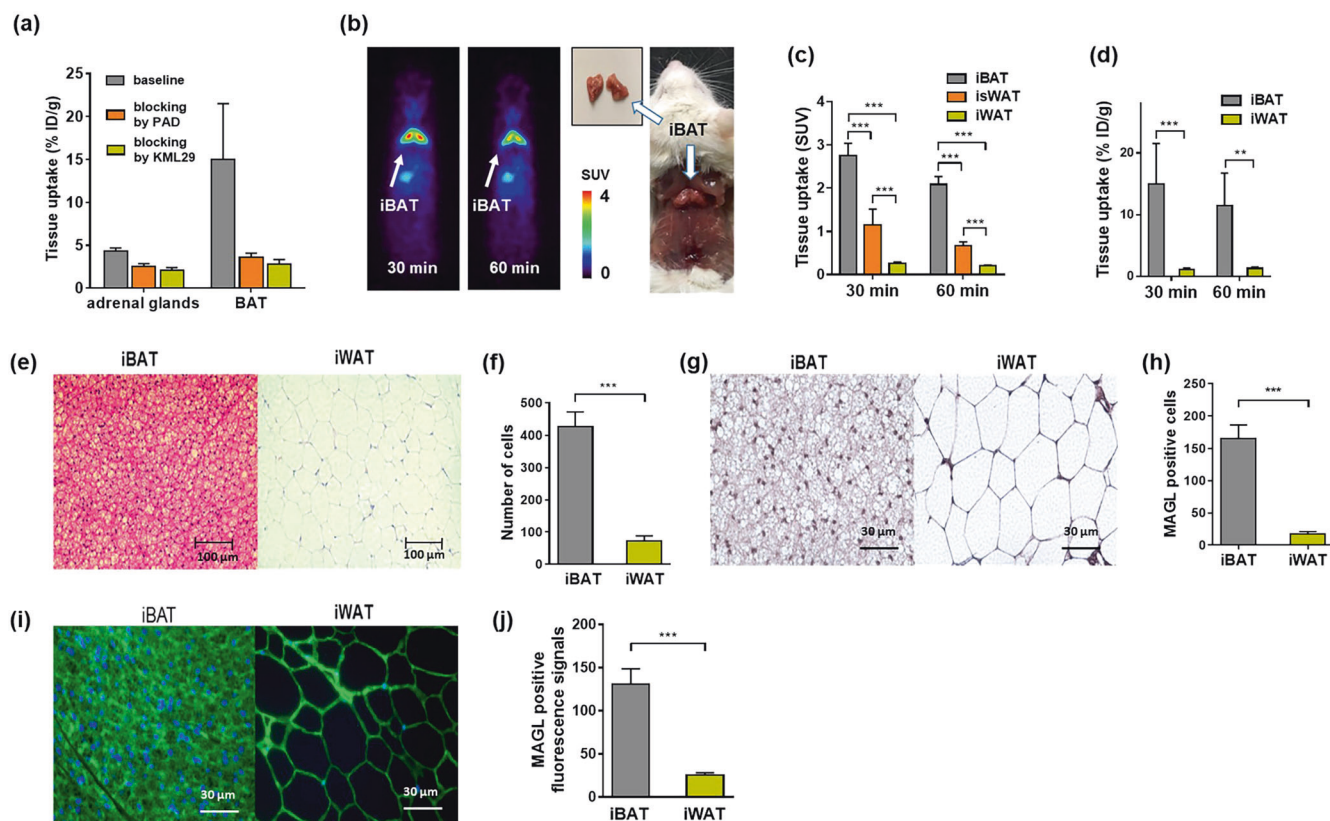
Fig. 4 **[18F]FEPAD ([18F]4) is a specific MAGL PET ligand that selectively discriminates BAT from WAT. a** Uptake of [18F]FEPAD in adrenal glands and iBAT determined by ex vivo distribution under baseline and blocking conditions (PAD or KML29, 3 mg/kg, respectively); **b** Representative static PET images at 30 min and dissection photo of iBAT (arrow); **c** Tissue uptake (30 and 60 min) of [18F]FEPAD in iBAT, isWAT and iWAT determined by static PET imaging studies; **d** Ex vivo biodistribution (30 and 60 min) of [18F]FEPAD in iBAT and iWAT; **e** H&E staining and **f** quantitative measurement of adipocyte numbers in iBAT and iWAT. Scale bar, 100 μm; **g** MAGL immunohistochemistry and **h** quantification of MAGL expression in iBAT and iWAT. Slides were stained with NovaRED substrate that produces a brown-stain in MAGL protein, and they were counterstained with hematoxylin that results in blue-violet staining of nuclei. 40× magnification. Scale bar, 30 μm; **i** MAGL immunofluorescent staining and **j** fluorescence intensity in iBAT and iWAT. Slides were stained with an anti-MAGL antibody that produces a green-stain in MAGL protein, and they were counterstained with DAPI that results in blue-violet staining of nuclei. 40× magnification. Scale bar, 30 μm. iBAT interscapular BAT, isWAT interscapular WAT, iWAT inguinal WAT. All data were mean ± SD, $n = 3$-5. $^{**}P < 0.01$, and $^{***}P < 0.001$.

adipocytes from WAT were much larger in cell size than those from BAT. Quantitative measurement further indicated that the number of adipocytes from BAT was significantly higher (*ca.* 6 fold) than from WAT in the same size area (Fig. 4f). Along with the colocalization with the BAT, MAGL-positive protein staining was substantially higher in the BAT than WAT as evidenced both by immunohistochemistry (Fig. 4g) and immunofluorescence staining (Fig. 4i). Finally, BAT exhibited significantly higher MAGL density (*ca.* 5–10 fold) than WAT as shown in Fig. 4h, j, which corroborated the PET and ex vivo biodistribution findings.

DISCUSSION
In the present study, we reported on the development of a novel MAGL-targeted PET ligand, [18F]FEPAD, that is based on a unique 4-piperidinyl azetidine diamide scaffold and proved to be highly suitable for the non-invasive quantification of MAGL in the BAT. State-of-the-art tracer development revealed an outstanding in vitro and in vivo specificity as well as a remarkable selectivity for the BAT on small-animal PET images and by ex vivo biodistribution experiments. These findings were supported by a compound selectivity screening that revealed a > 100-fold selectivity over other major serine hydrolases, including FAAH, ABHD6, ABHD12, and KIAA1363, and CB_1/CB_2 receptors, and reversible binding profile towards MAGL. Post-mortem tissue analysis

underscored the utility of [18F]FEPAD for quantitative PET, thereby enabling a wide range of non-invasive mechanistic studies on the role of the endocannabinoid system in modulating metabolic BAT activity. Further, our findings shed light on the potential mechanisms underlying MAGL inhibition on lipid metabolism.

To date, most of developed MAGL PET molecules were labeled by the relatively short half-life carbon-11, which is not suitable for multistep synthesis and transportation. In the present work, we have prepared an F-18 labeled radioligand, [18F]FEPAD ([18F]4), that provides outstanding selectivity for MAGL-targeted imaging in the BAT and can be efficiently obtained in a two-step procedure by using 1-bromo-2-[18F]fluoroethane or 2-[18F]fluoroethyl tosylate with high RCY, radiochemical purity and molar activity (Fig. 3a).

MAGL was shown to be expressed in the BAT, adrenal gland, liver, brain, kidney and testis [37]. The ex vivo biodistribution of [18F]FEPAD was consistent with the distribution of MAGL. The observed high uptake in the BAT and low brain permeability revealed that [18F]FEPAD exhibits optimal performance characteristics for a peripheral MAGL PET radioligand (Fig. 3b). The specific binding studies also indicate [18F]FEPAD is a superior PET ligand to reported C-11 labeled [11C]PAD with higher specific binding to MAGL. WAT stores excess energy, and is present in several locations throughout the body, mostly subcutaneously and intra-abdominally. Conversely, BAT is much less abundant and specialized in providing non-shivering thermogenesis and

A novel MAGL-targeted ^{18}F-labeled probe for PET imaging of BAT
R Cheng et al.

3009

dissipating energy as heat [40, 41]. Enhancing and activating BAT is recognized as a novel therapeutic approach to counteract cancer, neurodegeneration and metabolic diseases, including adiposity and obesity-associated diabetes [42–44]. Since the mass and percentage of BAT differs in individuals and cannot be determined externally, there is a critical demand to quantify BAT from abundant WAT for the diagnosis and prognosis of metabolic perturbations. More importantly, MAGL-based imaging not only serves to assess the mass of BAT, but also provides functional information on the amount of MAGL that is expressed in BAT. This crucial information is currently lacking in contemporary clinical practice, since non-invasive BAT assessment is primarily conducted with the non-specific probe, [18F]fluorodeoxyglucose ([18F] FDG) PET. Of note, recent studies indicated that the endocannabinoid system (ECS) plays a central role in the metabolic function of adipose tissues as a regulator, which has prompted a wave of enthusiasm and triggered various research programs in academia and the pharmaceutical industry [45–47]. Considering that CB_1 receptors seem to be colocalized with uncoupling protein-1 in BAT [48], a proof-of-concept application with a suitable MAGL-targeted probe is of paramount value to elucidate how the ECS is linked to BAT-related metabolic disorders. We now provide evidence that non-invasive assessment of MAGL expression in BAT is feasible with PET, thereby enabling a wide array of mechanistic studies with [18F]FEPAD and raising awareness of the potential translational relevance of MAGL in metabolic disorders.

In summary, we have developed a novel F-18 labeled MAGL PET probe, [18F]FEPAD (also named as [18F]**4**), based on a unique piperidinyl azetidine amide scaffold that is suited for non-invasive quantification of MAGL in the BAT. This probe not only represented specific and reversible binding mechanism to MAGL, but also demonstrated its promise for selectively discriminating between BAT and WAT deposits. We have corroborated imaging findings with post-mortem tissue analysis, which underscored the suitability of [18F]FEPAD to specifically and selectively visualize MAGL. Our discovery would extend the understanding of MAGL in the peripheral ECS and provide a new surrogate PET biomarker for functional BAT imaging, thereby providing a unique tool to study metabolic disorders non-invasively. The availability of such a tool in the clinic would substantially improve our understanding of the role of the ECS in metabolic disorders.

AUTHOR CONTRIBUTIONS
RC and SHL designed the research; RC, MF, JY, JR AH, DO, RSV, TS, ZC, XZ, ERCL, YZ, WM, KK, TY and LX performed research; RC analyzed the data; RC and SHL wrote the paper; SS, LW, CR, YS, BC, LJ, MRZ and SHL conceived and reviewed the paper.

ADDITIONAL INFORMATION
Supplementary information The online version contains supplementary material available at https://doi.org/10.1038/s41401-022-00912-8.

Competing interests: The authors declare no competing interests.

Ethical approval: All applicable international, national, and/or institutional guidelines for the care and use of animals were followed.

REFERENCES
1. Nomura DK, Morrison BE, Blankman JL, Long JZ, Kinsey SG, Marcondes MC, et al. Endocannabinoid hydrolysis generates brain prostaglandins that promote neuroinflammation. Science. 2011;334:809–13.
2. Piro JR, Benjamin DI, Duerr JM, Pi Y, Gonzales C, Wood KM, et al. A dysregulated endocannabinoid-eicosanoid network supports pathogenesis in a mouse model of Alzheimer's disease. Cell Rep. 2012;1:617–23.
3. Chen R, Zhang J, Wu Y, Wang D, Feng G, Tang YP, et al. Monoacylglycerol lipase is a therapeutic target for Alzheimer's disease. Cell Rep. 2012;2:1329–39.
4. Mulvihill MM, Nomura DK. Therapeutic potential of monoacylglycerol lipase inhibitors. Life Sci. 2013;92:492–7.
5. Griebel G, Pichat P, Beeske S, Leroy T, Redon N, Jacquet A, et al. Selective blockade of the hydrolysis of the endocannabinoid 2-arachidonoylglycerol impairs learning and memory performance while producing antinociceptive activity in rodents. Sci Rep. 2015;5:7642.
6. Pacher P, Batkai S, Kunos G. The endocannabinoid system as an emerging target of pharmacotherapy. Pharmacol Rev. 2006;58:389–462.
7. Pagotto U, Marsicano G, Cota D, Lutz B, Pasquali R. The emerging role of the endocannabinoid system in endocrine regulation and energy balance. Endocr Rev. 2006;27:73–100.
8. Matias I, Di Marzo V. Endocannabinoids and the control of energy balance. Trends Endocrinol Metab. 2007;18:27–37.
9. Bifulco M, Laezza C, Gazzerro P, Pentimalli F. Endocannabinoids as emerging suppressors of angiogenesis and tumor invasion (review). Oncol Rep. 2007;17:813–6.
10. Long JZ, Nomura DK, Cravatt BF. Characterization of monoacylglycerol lipase inhibition reveals differences in central and peripheral endocannabinoid metabolism. Chem Biol. 2009;16:744–53.
11. Nomura DK, Long JZ, Niessen S, Hoover HS, Ng SW, Cravatt BF. Monoacylglycerol lipase regulates a fatty acid network that promotes cancer pathogenesis. Cell. 2010;140:49–61.
12. Grimsey NL, Savinainen JR, Attili B, Ahamed M. Regulating membrane lipid levels at the synapse by small-molecule inhibitors of monoacylglycerol lipase: new developments in therapeutic and PET imaging applications. Drug Discov Today. 2020;25:330–43.
13. Hicks JW, Parkes J, Tong J, Houle S, Vasdev N, Wilson AA. Radiosynthesis and ex vivo evaluation of [11C-carbonyl]carbamate- and urea-based monoacylglycerol lipase inhibitors. Nucl Med Biol. 2014;41:688–94.
14. Hou L, Rong J, Haider A, Ogasawara D, Varlow C, Schafroth MA, et al. Positron emission tomography imaging of the endocannabinoid system: opportunities and challenges in radiotracer development. J Med Chem. 2021;64:123–49.
15. Innis RB, Cunningham VJ, Delforge J, Fujita M, Gjedde A, Gunn RN, et al. Consensus nomenclature for in vivo imaging of reversibly binding radioligands. J Cereb Blood Flow Metab. 2007;27:1533–9.
16. Pike VW. PET radiotracers: crossing the blood-brain barrier and surviving metabolism. Trends Pharmacol Sci. 2009;30:431–40.
17. Hattori Y, Aoyama K, Maeda J, Arimura N, Takahashi Y, Sasaki M, et al. Design, synthesis, and evaluation of (4R)-1-{3-[2-(18F)fluoro-4-methylpyridin-3-yl]phenyl}-4-[4-(1,3-thiazol-2-ylcarbonyl)piperazin-1-yl]pyrrolidin-2-one ([18F]T-401) as a novel positron-emissiontomography imaging agent for monoacylglycerol lipase. J Med Chem. 2019;62:2362–75.
18. Chen Z, Mori W, Deng X, Cheng R, Ogasawara D, Zhang G, et al. Design, synthesis, and evaluation of reversible and irreversible monoacylglycerol lipase positron emission tomography (PET) tracers using a "tail switching" strategy on a piperazinyl azetidine skeleton. J Med Chem. 2019;62:3336–53.
19. Rong J, Mori W, Xia X, Schafroth MA, Zhao C, Van RS, et al. Novel reversible-binding PET ligands for imaging monoacylglycerol lipase based on the piperazinyl azetidine scaffold. J Med Chem. 2021;64:14283–98.
20. Deng X, Rong J, Wang L, Vasdev N, Zhang L, Josephson L, et al. Chemistry for positron emission tomography: recent advances in [11]C-, [18]F-, [13]N-, and ^{15}O-labeling reactions. Angew Chem Int Ed. 2019;58:2580–605.
21. Lahesmaa M, Eriksson O, Gnad T, Oikonen V, Bucci M, Hirvonen J, et al. Cannabinoid type 1 receptors are upregulated during acute activation of brown adipose tissue. Diabetes. 2018;67:1226–36.
22. Calderon-Dominguez M, Mir JF, Fucho R, Weber M, Serra D, Herrero L. Fatty acid metabolism and the basis of brown adipose tissue function. Adipocyte. 2015;5:98–118.
23. Deng H, Li W. Monoacylglycerol lipase inhibitors: modulators for lipid metabolism in cancer malignancy, neurological and metabolic disorders. Acta Pharm Sin B. 2020;10:582–602.
24. Wang L, Mori W, Cheng R, Yui J, Hatori A, Ma L, et al. Synthesis and preclinical evaluation of sulfonamido-based [11C-Carbonyl]-carbamates and ureas for imaging monoacylglycerol lipase. Theranostics. 2016;6:1145–59.
25. Blankman JL, Simon GM, Cravatt BF. A comprehensive profile of brain enzymes that hydrolyze the endocannabinoid 2-arachidonoylglycerol. Chem Biol. 2007;14:1347–56.
26. Cheng R, Mori W, Ma L, Alhouayek M, Hatori A, Zhang Y, et al. In vitro and in vivo evaluation of ^{11}C-labeled azetidinecarboxylates for imaging monoacylglycerol lipase by PET imaging studies. J Med Chem. 2018;61:2278–91.

A novel MAGL-targeted ^{18}F-labeled probe for PET imaging of BAT
R Cheng et al.

3010

27. Cravatt BF, Wright AT, Kozarich JW. Activity-based protein profiling: from enzyme chemistry to proteomic chemistry. Annu Rev Biochem. 2008;77:383–414.

28. Wang L, Cheng R, Fujinaga M, Yang J, Zhang Y, Hatori A, et al. A facile radio-labeling of [^{18}F]FDPA via spirocyclic iodonium ylides: preliminary PET imaging studies in preclinical models of neuroinflammation. J Med Chem. 2017;60:5222–7.

29. Zhang X, Kumata K, Yamasaki T, Cheng R, Hatori A, Ma L, et al. Synthesis and preliminary studies of a novel negative allosteric modulator, 7-((2,5-Dioxopyrro-lidin-1-yl)methyl)-4-(2-fluoro-4-[^{11}C]methoxyphenyl) quinoline-2-carboxamide, for imaging of metabotropic glutamate receptor 2. ACS Chem Neurosci. 2017;8:1937–48.

30. Wang S, Lee Y, Kim J, Hyun J, Lee K, Kim Y, et al. Potential role of hedgehog pathway in liver response to radiation. PLoS One. 2013;8:e74141.

31. Kim J, Wang S, Hyun J, Choi SS, Cha H, Ock M, et al. Hepatic stellate cells express thymosin beta 4 in chronically damaged liver. PLoS One. 2015;10:e0122758.

32. Goodpaster T, Randolph-Habecker J. A flexible mouse-on-mouse immunohisto-chemical staining technique adaptable to biotin-free reagents, immuno-fluorescence, and multiple antibody staining. J Histochem Cytochem. 2014;62:197–204.

33. Campbell EL, Bruyninckx WJ, Kelly CJ, Glover LE, McNamee EN, Bowers BE, et al. Transmigrating neutrophils shape the mucosal microenvironment through localized oxygen depletion to influence resolution of inflammation. Immunity. 2014;40:66–77.

34. Wang L, Fujinaga M, Cheng R, Yui J, Shimoda Y, Rotstein BH, et al. Synthesis and preliminary evaluation of a ^{11}C-labeled piperidin-4-yl azetidine diamide for imaging monoacylglycerol lipase. J Nucl Med. 2016;57:1044.

35. Friesner RA, Banks JL, Murphy RB, Halgren TA, Klicic JJ, Mainz DT, et al. Glide: a new approach for rapid, accurate docking and scoring. 1. method and assessment of docking accuracy. J Med Chem. 2004;47:1739–49.

36. Halgren TA, Murphy RB, Friesner RA, Beard HS, Frye LL, Pollard WT, et al. Glide: a new approach for rapid, accurate docking and scoring. 2. enrichment factors in database screening. J Med Chem. 2004;47:1750–9.

37. Karlsson M, Contreras JA, Hellman U, Tornqvist H, Holm C. cDNA cloning, tissue distribution, and identification of the catalytic triad of monoglyceride lipase.

38. Chang JW, Niphakis MJ, Lum KM, Cognetta AB 3rd, Wang C, Matthews ML, et al. Highly selective inhibitors of monoacylglycerol lipase bearing a reactive group that is bioisosteric with endocannabinoid substrates. Chem Biol. 2012;19:579–88.

Evolutionary relationship to esterases, lysophospholipases, and haloperoxidases. J Biol Chem. 1997;272:27218–23.

39. Zhang X, Kuo C, Moore A, Ran C. In vivo optical imaging of interscapular brown adipose tissue with ^{18}F-FDG via Cerenkov Luminescence Imaging. PLoS One. 2013;8:e62007.

40. Cannon B, Nedergaard J. Brown adipose tissue: function and physiological significance. Physiol Rev. 2004;84:277–359.

41. Nielsen TS, Jessen N, Jørgensen JOL, Møller N, Lund S. Dissecting adipose tissue lipolysis: molecular regulation and implications for metabolic disease. J Mol Endocrinol. 2014;52:R199–R222.

42. Cypess AM, Kahn CR. Brown fat as a therapy for obesity and diabetes. Curr Opin Endocrinol Diabetes Obes. 2010;17:143–9.

43. Parimisetty A, Dorsemans AC, Awada R, Ravanan P, Diotel N, Lefebvre d'Hellen-court C. Secret talk between adipose tissue and central nervous system via secreted factors—an emerging frontier in the neurodegenerative research. J Neuroinflammation. 2016;13:67–79.

44. Vaitkus JA, Celi FS. The role of adipose tissue in cancer-associated cachexia. Exp Biol Med. 2017;242:473–81.

45. Silvestri C, Di, Marzo V. The endocannabinoid system in energy homeostasis and the etiopathology of metabolic disorders. Cell Metab. 2013;17:475–90.

46. Isabelle M, Ilaria B, Daniela C. The fat side of the endocannabinoid system: role of endocannabinoids in the adipocyte. Cannabis Cannabinoid Res. 2016;1:176–85.

47. van Eenige R, van der Stelt M, Rensen PCN, Kooijman S. Regulation of adipose tissue metabolism by the endocannabinoid system. Trends Endocrinol Metab. 2018;29:326–37.

48. Eriksson O, Mikkola K, Espes D, Tuominen L, Virtanen K, Forsback S, et al. The cannabinoid receptor-1 is an imaging biomarker of brown adipose tissue. J Nucl Med. 2015;56:1937–41.